Temporal mode sorting using dual-stage quantum frequency conversion by asymmetric Bragg scattering

Christensen, Jesper Bjerge; Reddy, Dileep V.; McKinstrie, C. J.; Rottwitt, Karsten; Raymer, M. G.

Published in:
Optics Express

Link to article, DOI:
10.1364/oe.23.023287

Publication date:
2015

Document Version
Publisher's PDF, also known as Version of record

Temporal mode sorting using dual-stage quantum frequency conversion by asymmetric Bragg scattering

Jesper B. Christensen,[1,2] Dileep V. Reddy,[2] C. J. McKinstrie,[3] K. Rottwitt,[1] and M. G. Raymer[2,*]

[1]*Department of Photonics Engineering, Technical University of Denmark, DK-2800 Kgs. Lyngby, Denmark*

[2]*Oregon Center for Optics, Department of Physics, University of Oregon, Eugene, Oregon 97403, USA*

[3]*Applied Communication Sciences, Red Bank, New Jersey 07701, USA*

[*]*raymer@uoregon.edu*

Abstract: The temporal shape of single photons provides a high-dimensional basis of temporal modes, and can therefore support quantum computing schemes that go beyond the qubit. However, the lack of linear optical components to act as quantum gates has made it challenging to efficiently address specific temporal-mode components from an arbitrary superposition. Recent progress towards realizing such a "quantum pulse gate," has been proposed using nonlinear optical signal processing to add coherently the effect of multiple stages of quantum frequency conversion. This scheme, called temporal-mode interferometry [D. V. Reddy, Phys. Rev. A **91**, 012323 (2015)], has been shown in the case of three-wave mixing to promise near-unity mode-sorting efficiency. Here we demonstrate that it is also possible to achieve high mode-sorting efficiency using four-wave mixing, if one pump pulse is long and the other short — a configuration we call asymmetrically-pumped Bragg scattering.

OCIS codes: (270,5585) Quantum information and processing; (190.4380) Nonlinear optics, four-wave mixing; (070.4340) Nonlinear optical signal processing; (060.4230) Multiplexing.

References and links

1. B. Brecht, D. V. Reddy, C. Silberhorn, and M. G. Raymer, "Photon temporal modes: a complete framework for quantum information science," http://arxiv.org/abs/1504.06251 (2015).
2. J. T. Barreiro, T. C. Wei, and P. G. Kwiat, "Beating the channel capacity limit for linear photonic superdense coding," Nat. Phys. **4**, 282–286 (2008).
3. B. Brecht, A. Eckstein, R. Ricken, V. Quiring, H. Suche, L. Sansoni, and C. Silberhorn, "Demonstration of coherent time-frequency Schmidt mode selection using dispersion-engineered frequency conversion," Phys. Rev. A **90**, 030302 (2014).
4. H. J. McGuinness, M. G. Raymer, and C. J. McKinstrie, "Theory of quantum frequency translation of light in optical fiber: application to interference of two photons of different color," Opt. Express **19**, 17876–17907 (2011).
5. A. Eckstein, B. Brecht, and C. Silberhorn, "A quantum pulse gate based on spectrally engineered sum frequency generation," Opt. Express **19**, 13770–13778 (2011).
6. D. V. Reddy, M. G. Raymer, C. J. McKinstrie, L. Mejling, and K. Rottwitt, "Temporal mode selectivity by frequency conversion in second-order nonlinear optical waveguides," Opt. Express **21**, 13840–13863 (2013).
7. J. Huang and P. Kumar, "Observation of quantum frequency conversion," Phys. Rev. Lett. **68**(14), 2153 (1992).

#243459 Received 23 Jun 2015; revised 17 Aug 2015; accepted 17 Aug 2015; published 26 Aug 2015

8. D. V. Reddy, M. G. Raymer, and C. J. McKinstrie, "Efficient sorting of quantum-optical wave packets by temporal-mode interferometry," Opt. Lett. **39**, 2924–2927 (2014).
9. D. V. Reddy, M. G. Raymer, and C. J. McKinstrie, "Sorting photon wave packets using temporal-mode interferometry based on multiple-stage quantum frequency conversion," Phys. Rev. A **91**, 012323 (2015).
10. L. Mejling, S. M. M. Friis, D. V. Reddy, K. Rottwitt, M. G. Raymer, and C. J. McKinstrie, "Asymmetrically pumped Bragg scattering with the effects of nonlinear phase modulation," in *Advanced Photonics*, (Optical Society of America, 2014), paper JTu3A.36.
11. N. K. Langford, S. Ramelow, R. Prevedel, W. J. Munro, G. J. Milburn, and A. Zeilinger, "Efficient quantum computing using coherent photon conversion," Nature (London) **478**(7369), 360–363 (2011).
12. G. P. Agrawal, *Nonlinear Fiber Optics*, , 5th ed. (Academic, 2013).
13. R. Giacone, C. McKinstrie, and R. Betti, "Angular dependence of stimulated Brillouin scattering in homogeneous plasma," Phys. Plasmas 2, 4596–4605 (1995).
14. H. J. McGuinness, M. G. Raymer, C. J. McKinstrie, and S. Radic, "Quantum frequency translation of single-photon states in a photonic crystal fiber," Phys. Rev. Lett. **105**, 093604 (2010).
15. C. J. McKinstrie, L. Mejling, M. G. Raymer, and K. Rottwitt, "Quantum-state-preserving optical frequency conversion and pulse reshaping by four-wave mixing," Phys. Rev. A **85**, 053829 (2012).
16. L. Mejling, D. S. Cargill, C. J. McKinstrie, K. Rottwitt, and R. O. Moore, "Effects of nonlinear phase modulation on Bragg scattering in the low-conversion regime," Opt. Express **20**, 27454–27475 (2012).
17. L. Mejling, C. J. McKinstrie, M. G. Raymer, and K. Rottwitt, "Quantum frequency translation by four-wave mixing in a fiber: low-conversion regime," Opt. Express **20**, 8367–8396 (2012).
18. C. K. Law, I. A. Walmsley, and J. H. Eberly, "Continuous frequency entanglement: effective finite Hilbert space and entropy control," Phys. Rev. Lett. **84**, 5304–5307 (2000).
19. W. Wasilewski and M. G. Raymer, "Pairwise entanglement and readout of atomic-ensemble and optical wavepacket modes in traveling-wave Raman interactions," Phys. Rev. A **73**, 063816 (2006).
20. M. G. Raymer, S. J. van Enk, C. J. McKinstrie, and H. J. McGuinness, "Interference of two photons of different color," Opt. Commun. **283**, 747–752 (2010).
21. S. Clemmen, A. Farsi, S. Ramelow, and A. L. Gaeta, "Ramsey interferometry with photons," in Proceedings of *CLEO: 2014 Postdeadline Paper Digest*, (Optical Society of America, 2014), paper FTh5A.2.

1. Introduction

Constructing efficient classical and quantum optical networks requires using all of the degrees of freedom of light. Recent studies have proposed using temporally and spectrally overlapping field-orthogonal optical wave packets, called temporal modes (TMs), to encode information [1]. In classical optical networks, the TMs allow for a new method of multiplexing, and can therefore aid in meeting the increasing demands for the flexible use of bandwidth. In quantum optical networks the infinite-dimensional space spanned by TMs make them ideal for high-dimensional quantum computing [2, 3]. An essential tool for enabling networks using TMs is the quantum pulse gate, which is a device that separates user-specified TMs through the pulse-selective nature of nonlinear-optical frequency conversion [4–6]. More specifically, a quantum pulse gate utilizes either three-wave mixing in second-order nonlinear media or four-wave mixing (FWM) in third-order nonlinear media, to frequency convert a target TM with high fidelity. The frequency converted TM component is subsequently separated using a linear optical element such as a dichroic mirror, and maintains any initial quantum entanglement possessed prior to the quantum pulse gate [7].

Near-100% TM selectivity is predicted for frequency conversion by multi-stage three-wave mixing in second-order nonlinear optical waveguides [8, 9]. This scheme is called temporal-mode interferometry (TMI) [8]. The question posed in the present study is whether comparable TM selectivity can also be achieved using frequency conversion by multi-stage nondegenerate FWM in optical fiber.

The challenge in the case of FWM is that nonlinear phase modulation (NPM) of the two signal frequency channels, as well as the two pump laser pulses, introduces undesirable temporal phase structure that degrades the TM selectivity of the process. In principle, this issue can be overcome by pre-chirping the two pump laser pulses with the aim of attaining control of the signal temporal phase profiles [9]. However, implementing the required pre-chirps would

#243459 Received 23 Jun 2015; revised 17 Aug 2015; accepted 17 Aug 2015; published 26 Aug 2015

inevitably increase the complexity of the quantum pulse gate device. Here we propose that by using a combination of a weak, short pump pulse and a strong, broad pump field, the unwanted effects of NPM can be eliminated while retaining high TM selectivity. The shape of the weak, short pulse defines the target TM, while the strong, constant field creates only a constant change of the effective refractive index. We predict that this scheme, which we call asymmetrically-pumped Bragg scattering, will imitate the three-wave mixing process, as the NPM effects can be accounted for by merely frequency shifting the pump pulses [10]. Asymmetrically-pumped Bragg scattering may be utilized in nonlinear optic quantum computing schemes by realizing deterministic photon-photon interaction such as coherent photon conversion [11].

Compared to second-order crystalline wave-guide implementations, a fiber-based quantum pulse gate would have the advantages of (i) compatibility with current communication technologies in terms of transverse fiber modes, (ii) versatility by allowing both large and small frequency translations, and (iii) applicability to signal pulse durations ranging from sub-picoseconds to tens-of-ps, whereas second-order implementations are limited to sub-picosecond signals due to the available length of crystalline wave-guides.

By using analytical and numerical techniques, we verify that a highly selective quantum pulse gate can be designed using this asymmetrically-pumped multi-stage scheme. We discuss how the TM selectivity depends on the different physical parameters, and present a specific example of feasible parameters that results in near ideal performance of the quantum pulse gate.

2. Theory of asymmetrically-pumped Bragg scattering

We consider the nondegenerate form of FWM called Bragg scattering (BS), which includes two pumps p, q and two weak (quantum) signals r, s with carrier frequencies obeying $\omega_p + \omega_s = \omega_q + \omega_r$. In this process, which is illustrated in Fig. 1, photons are conventionally annihilated in pairs from p, s and created in pairs in q, r (or reversely). Assuming perfect phase-matching the coupled-mode equations governing the evolution of the slowly varying field envelopes A_j of units $\mathrm{W}^{1/2}$ in an optical waveguide are [12]

$$\left(\partial_z + \beta_p^{(1)}\partial_t\right) A_p = i\gamma\left(|A_p|^2/2 + |A_q|^2\right) A_p, \tag{1a}$$

$$\left(\partial_z + \beta_q^{(1)}\partial_t\right) A_q = i\gamma\left(|A_p|^2 + |A_q|^2/2\right) A_q, \tag{1b}$$

$$\left(\partial_z + \beta_s^{(1)}\partial_t\right) A_s = i\gamma\left(|A_p|^2 + |A_q|^2\right) A_s + i\gamma A_p^* A_q A_r, \tag{1c}$$

$$\left(\partial_z + \beta_r^{(1)}\partial_t\right) A_r = i\gamma\left(|A_p|^2 + |A_q|^2\right) A_r + i\gamma A_p A_q^* A_s, \tag{1d}$$

where $\partial_z \equiv \partial/\partial z$, $\partial_t \equiv \partial/\partial t$, $\beta_j^{(1)} = (\partial\beta(\omega)/\partial\omega)|_{\omega=\omega_j}$ is the inverse group speed of the jth field, and $\gamma = 2\gamma_K$ where γ_K is the nonlinear Kerr coefficient in units of $\mathrm{W}^{-1}\,\mathrm{m}^{-1}$, which is assumed to be frequency independent. The coupled-mode equations can be interpreted quantum mechanically by making the substitutions $A_{r,s} \to \hat{a}_{r,s}$, where the creation and annihilation operators obey the commutation relation $[\hat{a}_j(t,z), \hat{a}_k^\dagger(t',z')] = \delta(t-t')\delta(z-z')\delta_{jk}$, where $\delta(x)$ is the Dirac delta-function and δ_{jk} is the Kronecker delta-function. In arriving at Eq. (1), intra-pulse dispersion, fiber losses, nonlinear scattering mechanisms (Brillouin and Raman), and polarization effects were neglected.

In the context of asymmetrically-pumped BS, which is the focus here, pump p is a continuous-wave (CW) or quasi-CW field which is much stronger than the pulsed pump q. This enables us to ignore the time-dependent NPM terms originating from pump q, as these are only weak perturbations to the NPM terms from pump p, which merely modify the wavenumber

#243459 Received 23 Jun 2015; revised 17 Aug 2015; accepted 17 Aug 2015; published 26 Aug 2015

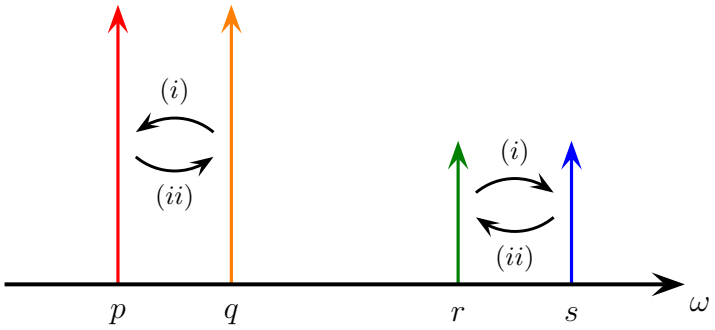

Fig. 1. Schematic of the interacting fields in near conversion Bragg scattering. The curved arrows indicate photon transfer illustrated for (i) signal up-conversion, and (ii) signal down-conversion.

matching condition. The coupled-mode equations then reduce to

$$\partial_z A_p = i\gamma |A_p|^2 A_p/2, \tag{2a}$$

$$\left(\partial_z + \beta_q^{(1)}\partial_t\right) A_q = i\gamma |A_p|^2 A_q, \tag{2b}$$

$$\left(\partial_z + \beta_s^{(1)}\partial_t\right) A_s = i\gamma |A_p|^2 A_s + i\gamma A_p^* A_q A_r, \tag{2c}$$

$$\left(\partial_z + \beta_r^{(1)}\partial_t\right) A_r = i\gamma |A_p|^2 A_r + i\gamma A_p A_q^* A_s, \tag{2d}$$

where it has been exploited that pump p is a CW field. In Sec. 4, we show by numerical estimates that there is a practically achievable regime in which the stated assumptions are valid to a good approximation.

Since the signals are weak, the pump equations are effectively decoupled from the equations governing the signal evolution, and can thus be solved independently with the solutions

$$A_p(z) = a_p(0)\exp\left(i\gamma P_p z/2\right), \qquad A_q(z,t) = a_q(t-\beta_q z)\exp\left(i\gamma P_p z\right), \tag{3}$$

where $P_p = |a_p(0)|^2$ is the power of pump p at the input point $z = 0$, and we have introduced the abbreviated notation $\beta_j \equiv \beta_j^{(1)}$.

The solution to the part of the coupled-mode equations describing the evolution of the signals can be expressed in the input-output form

$$A_j(l,t) = \sum_{k=s,r} \int_{-\infty}^{\infty} \mathrm{d}t'\, G_{jk}(t,t') A_k(0,t'), \qquad (j = s,r), \tag{4}$$

where t' is to be referred to as the input time, t the output time, and $G_{jk}(t,t') \equiv G_{jk}(l,t|0,t')$ are the Green function (GF) kernels which transform the input in mode k to the output in mode j at the fiber output $z = l$. The GF kernels depend on the fiber parameters γ, l, β_j as well as the shape and strength of the two pumps, and in the optimal case [6] where the group velocities are matched according to $\beta_q = \beta_r \neq \beta_s$, the GF kernels can be found analytically [13]. In practice, this group-velocity matching can be realized by using certain photonic crystal fibers, while placing the interacting fields symmetrically around a zero-dispersion frequency to

#243459 Received 23 Jun 2015; revised 17 Aug 2015; accepted 17 Aug 2015; published 26 Aug 2015

achieve phase matching [14]. Assuming without loss of generality that $\beta_r > \beta_s$, the GF kernels for asymmetrically-pumped BS are

$$G_{rr}(t,t') = \Bigg[\mathrm{H}(t-t'-\beta_s l)\,\delta(t'-t+\beta_r l)\left(\frac{a_q(t-\beta_r l)}{a_q(t')}\right)^* - \bar{\gamma}\left(\frac{\eta(t,t')}{\xi(t,t')}\right)^{1/2} a_q^*(t-\beta_r l)\,\mathrm{J}_1\left\{2\bar{\gamma}\left[\eta(t,t')\xi(t,t')\right]^{1/2}\right\} a_q(t') \times \mathrm{H}(t'-t+\beta_r l)\,\mathrm{H}(t-t'-\beta_s l)\Bigg] \exp\left[i\Gamma_p\left(t-t'+\beta_r l-2\beta_s l\right)\right], \tag{5}$$

$$G_{rs}(t,t') = i\bar{\gamma}a_q^*(t-\beta_r l)\mathrm{J}_0\left\{2\bar{\gamma}\left[\eta(t,t')\xi(t,t')\right]^{1/2}\right\} a_p(t') \times \mathrm{H}(t'-t+\beta_r l)\,\mathrm{H}(t-t'-\beta_s l)\exp\left[i\Gamma_p\left(t-t'+\beta_r l-2\beta_s l\right)\right], \tag{6}$$

$$G_{sr}(t,t') = i\bar{\gamma}a_p^*(t)\mathrm{J}_0\left\{2\bar{\gamma}\left[\eta(t,t')\xi(t,t')\right]^{1/2}\right\} a_q(t') \times \mathrm{H}(t'-t+\beta_r l)\,\mathrm{H}(t-t'-\beta_s l)\exp\left[i\Gamma_p\left(t-t'+2\beta_r l-3\beta_s l\right)\right], \tag{7}$$

$$G_{ss}(t,t') = \Bigg[\mathrm{H}(t'-t+\beta_r l)\,\delta(t-t'-\beta_s l)\left(\frac{a_p(t)}{a_p(t')}\right)^* - \bar{\gamma}\left(\frac{\xi(t,t')}{\eta(t,t')}\right)^{1/2} a_p^*(t)\,\mathrm{J}_1\left\{2\bar{\gamma}\left[\eta(t,t')\xi(t,t')\right]^{1/2}\right\} a_p(t') \times \mathrm{H}(t'-t+\beta_r l)\,\mathrm{H}(t-t'-\beta_s l)\Bigg] \exp\left[i\Gamma_p\left(t-t'+2\beta_r l-3\beta_s l\right)\right], \tag{8}$$

where $\bar{\gamma} = \gamma/(\beta_r-\beta_s) = \gamma/\beta_{rs}$, $\Gamma_p = \bar{\gamma}P_p/2$ is a parameter with units of frequency, J_n is the nth order Bessel function of the first kind, H is the Heaviside step function, and the functions $\eta(t,t')$ and $\xi(t,t')$ are given as

$$\eta(t,t') = \left(t-t'-\beta_s l\right)P_p, \qquad \xi(t,t') = \int_{t-\beta_r l}^{t'} \mathrm{d}\bar{t}\,|a_q(\bar{t})|^2. \tag{9}$$

The GF kernels found here are similar in form to those earlier presented for FWM BS [15, 16], and to those for three-wave mixing [6], apart from the exponential phase terms which are seen to be linear in both the input and output times.

We adopt the notation that β_r and β_s are to be measured relative to the average group slowness $\beta_{av} = (\beta_r+\beta_s)/2$, such that they obey $\beta_r = -\beta_s > 0$. Assuming pump q is a Gaussian pulse of energy E_q and e^{-1} intensity width τ_q, this notation enables us to put the GF kernels in a normalized form, e.g. for G_{rs}

$$G_{rs}(\tau,\tau') = \frac{i\gamma' a_q^*(\tau-\zeta)a_p(\tau')}{\sqrt{2\zeta}}\mathrm{J}_0\left\{\frac{\gamma'}{\sqrt{\zeta}}\sqrt{(\tau-\tau'+\zeta)\left[\mathrm{erf}\left(\tau'+\frac{\zeta}{2}\right)-\mathrm{erf}\left(\tau-\frac{\zeta}{2}\right)\right]}\right\} \times \mathrm{H}\left(\tau'-\tau+\zeta\right)\mathrm{H}\left(\tau-\tau'+\zeta\right)\exp\left[i\Gamma_p\tau_q\left(\tau-\tau'+3\zeta\right)\right], \tag{10}$$

where we have introduced the normalized times $\tau' = t'/\tau_q$, $\tau = t/\tau_q$, and defined the dimensionless interaction strength

$$\gamma' = \gamma\sqrt{\frac{P_p E_q l}{\beta_{rs}}}. \tag{11}$$

#243459 Received 23 Jun 2015; revised 17 Aug 2015; accepted 17 Aug 2015; published 26 Aug 2015

and the dimensionless inter-pulse walk-off distance

$$\zeta = \frac{\beta_{rs} l}{2\tau_q}, \tag{12}$$

The inter-pulse walk-off ζ determines the influence of the Heaviside functions which, when significant, prevent separability of the GF [17]. In the present case where a_p is of constant amplitude, the Heaviside functions never vanish as allowed by BS using two pulsed pumps in a full collision [15, 17]. However, as for three-wave mixing [6], by increasing ζ their influence can be diminished asymptotically.

3. Single-stage asymmetrically-pumped Bragg scattering

The GFs are complex kernels, each having their own singular value decomposition (or Schmidt decomposition) [18, 19]. The overall GF transform is unitary, and as a result the individual GF kernel Schmidt decompositions are related according to [20]

$$G_{rr}(t,t') = \sum_{n=1} \Psi_n(t)\tau_n\psi_n^*(t'), \tag{13a}$$

$$G_{rs}(t,t') = \sum_{n=1} \Psi_n(t)\rho_n\phi_n^*(t'), \tag{13b}$$

$$G_{sr}(t,t') = -\sum_{n=1} \Phi_n(t)\rho_n\psi_n^*(t'), \tag{13c}$$

$$G_{ss}(t,t') = \sum_{n=1} \Phi_n(t)\tau_n\phi_n^*(t'), \tag{13d}$$

where ψ_n, ϕ_n are the nth r, s-input Schmidt modes, Ψ_n, Φ_n are the nth r, s-output Schmidt modes, and ρ_n and τ_n are the nth order Schmidt coefficients, taken to be real without loss of generality. Within each set, the Schmidt modes are orthonormal satisfying the orthonormality condition

$$\int_{-\infty}^{\infty} \mathrm{d}t\ \psi_n(t)\psi_m^*(t) = \delta_{nm}, \tag{14}$$

with similar conditions satisfied for the other three sets of Schmidt modes. The Schmidt modes of the process define the optimal TMs of the surrounding quantum network, and thus, by engineering the Schmidt-mode shapes through the BS interaction, great TM flexibility is allowed.

One can interpret the Schmidt coefficients and Schmidt modes easily by considering the input-output form in Eq. (4) and the orthonormality condition in Eq. (14). Assume an input in the s-mode given by one of the nth Schmidt modes, i.e. $A_s(0,t') = \psi_n(t')$. The outputs are now $A_s(l,t) = \tau_n\Phi_n(t)$ for the s-mode and $A_r(l,t) = \rho_n\Psi_n(t)$ for the r-mode. From this it is readily seen that τ_n^2 is the transmission, i.e. non-conversion efficiency, and ρ_n^2 is the conversion efficiency (CE) of the nth input Schmidt mode, and they are probability conserving in the sense that $\tau_n^2 + \rho_n^2 = 1$ for each n.

Figure 2 shows the absolute values of the first two input and output Schmidt modes for both the r- and s-channels obtained using $\gamma' = 1.5$ and $\zeta = 20$. The Schmidt modes have been centered on the normalized time-axis to ease the comparison between input- and output modes. Considering the first-order Schmidt modes, the r-channel modes are shaped like pump q, while the s-channel modes mimic the flat shape of pump p, but are limited by the causality requirement to a temporal width of $\beta_{rs} l$. Thus, the s-channel Schmidt modes are approximately a factor 2ζ broader than the r-channel Schmidt modes. The s-channel Schmidt modes are merely used to drop (measure) a target TM, and the process does therefore not suffer from their non-typical temporal shape. The skewness of the first-order output Schmidt modes can be understood by considering a Gaussian input in the r-channel. The r-pulse overlaps with pump q throughout

#243459 Received 23 Jun 2015; revised 17 Aug 2015; accepted 17 Aug 2015; published 26 Aug 2015

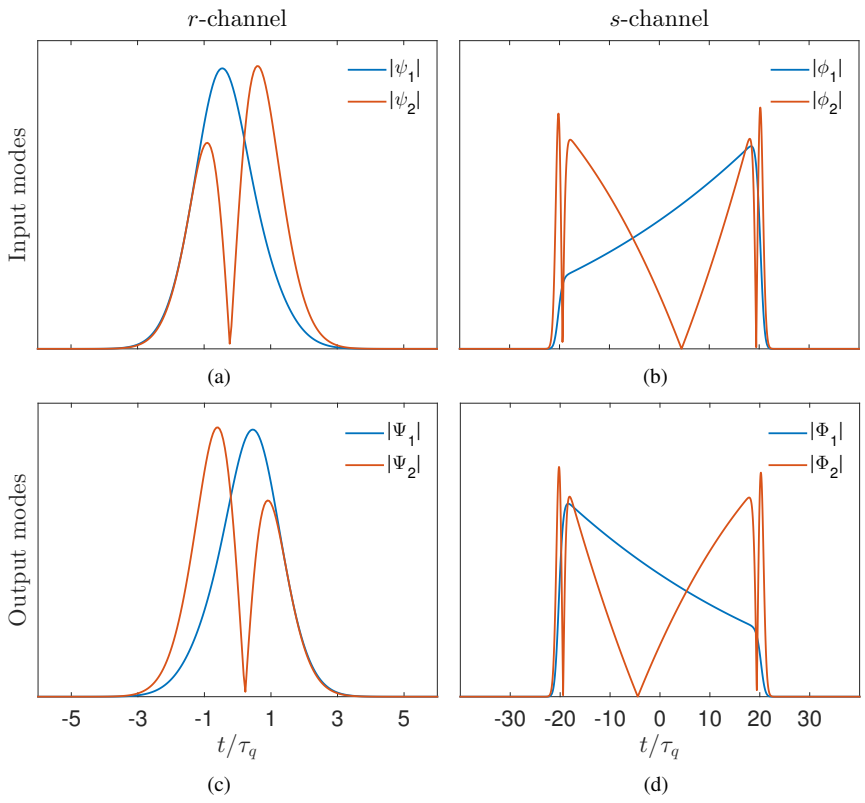

Fig. 2. The two lowest-order (first and second) (a) r-input, (b) s-input, (c) r-output, and (d) s-output Schmidt modes are shown for $\gamma' = 1.5$ and $\zeta = 20$.

the fiber length, and thus power is transferred to the s-channel continuously. The leading edge of the r-pulse interacts with a much stronger local s-signal than does the trailing edge of the r-pulse. Thus, the r-channel Schmidt mode is skewed toward the trailing edge. Conversely, the s-channel output mode is skewed toward the leading pulse edge by virtue of the increasingly depleted r-signal. The symmetry of this GF is apparent from the fact that each input Schmidt mode is skewed oppositely from its associated output Schmidt mode of same order.

Figure 3 shows values of Schmidt mode CEs for various values of γ' and ζ. The set of Schmidt coefficients ρ_n^2 belonging to the Schmidt modes in Fig. 2 are also seen as the circled points in Fig. 3. A general tendency is that increasing γ' increases the value of all ρ_n^2, whereas increasing ζ increases the value of the first Schmidt coefficient while reducing the values of the higher-order Schmidt coefficients. This last property can be explained by the reduced influence of the non-separable Heaviside functions as ζ is increased.

The performance of a quantum pulse gate device is characterized by its ability to frequency convert a target TM, while simultaneously transmitting all of the non-target TMs. The separability, defined as

$$\mathscr{S} = \frac{\rho_1^2}{\sum_n \rho_n^2} \leq 1, \tag{15}$$

describes the discrimination ability between different orders of Schmidt modes, and in the limit

#243459 Received 23 Jun 2015; revised 17 Aug 2015; accepted 17 Aug 2015; published 26 Aug 2015

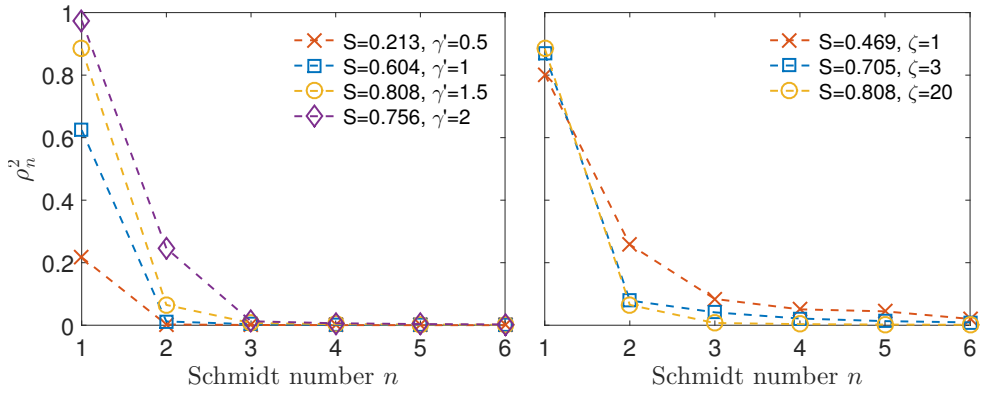

(a) (b)

Fig. 3. Single-stage Schmidt coefficients ρ_n^2 for (a) varying values of γ' and $\zeta = 20$, and (b) three different values of ζ for $\gamma' = 1.5$. The legends show the corresponding selectivities, S. Note that the lines labeled with circles are the same in the two figures, and are the Schmidt coefficients belonging to the Schmidt modes in Fig. 2.

where the Schmidt decomposition of the GF kernel contains only a single term, the separability is unity. A separability of unity is a necessary requirement for mode sorting, but it is not necessarily adequate. Consider the x-marked plot in Fig. 3(a). In this case $\rho_{n\geq 2}^2 \approx 0$, yielding a separability of unity, but the lowest-order Schmidt mode is converted with a CE of only ≈ 0.2. A more appropriate figure of merit is therefore the selectivity defined in [6],

$$S = \rho_1^2 \mathscr{S} = \frac{\rho_1^4}{\sum_n \rho_n^2} \leq 1, \tag{16}$$

which takes into account the CE of the first Schmidt mode. The selectivity is given in the legends in Fig. 3 with a maximum of $S = 0.808$ for $\gamma' = 1.5$ and $\zeta = 20$.

Figure 4(a) shows a more thorough investigation of the selectivity, which is plotted versus the dimensionless interaction strength γ' for four different values of the inter pulse walk-off ζ. As already indicated in Fig. 3, the selectivity increases with ζ. This effect is asymptotic for large values of ζ, and, as previously reported [3, 6, 15], the selectivity has an upper bound of $S_{\max} \approx 0.83$, as also found here for asymmetrically-pumped BS. Figure 4(b) shows the squared value of the three lowest Schmidt coefficients in the case $\zeta = 100$, which corresponds to the upper plot of Fig. 4(a). For sufficiently high nonlinearity ($\gamma' \approx 2$), the first-order Schmidt mode is converted with near 100 % efficiency, but the selectivity is low due to significant conversion of higher-order Schmidt modes. At around $\gamma' = 0.8$, the square of the first-order Schmidt coefficient is approximately 0.5, whereas those of the higher-order coefficients are still very small. It was this observation that inspired the introduction of a two-stage interferometric scheme called temporal-mode interferometry [8], which is considered next in the context of asymmetrically-pumped BS. TMI was introduced separately using CW fields, in which case there is no pulse-shape selectivity [21].

#243459 Received 23 Jun 2015; revised 17 Aug 2015; accepted 17 Aug 2015; published 26 Aug 2015

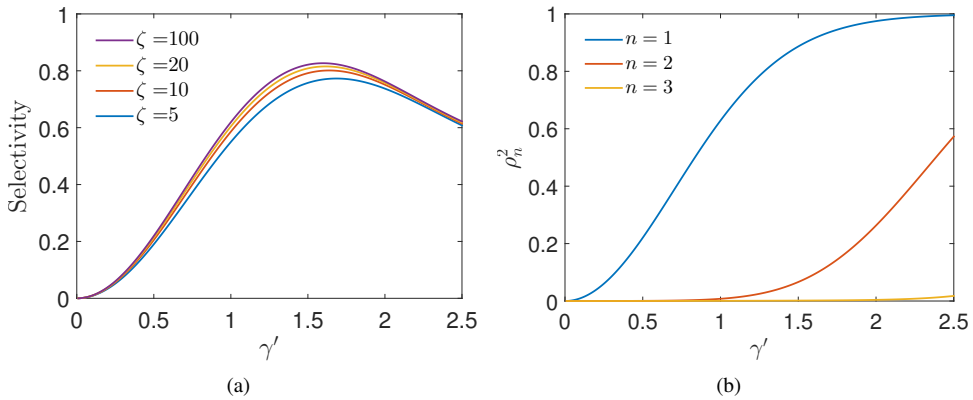

Fig. 4. (a) Single-stage selectivity versus the dimensionless interaction strength γ' for various values of ζ and (b) the evolution of the three lowest Schmidt coefficients for $\zeta = 100$.

4. Dual-stage asymmetrically-pumped Bragg scattering

TMI is conceptually similar to balanced Mach-Zender interferometry, in which an input given by a single-photon state is controlled by the relative phase between the two interferometer arms, to appear along either of the two output directions, with certainty. A good analogy can also be made to Ramsey dual-interaction interferometry [9, 21].

Figure 5 shows the schematic of a TMI setup using two cascaded stages of quantum frequency conversion (QFC). The input is placed in the *r*-channel (green) and is in this example a superposition of three TMs. Pump *p* (red) is the CW-pump, and pump *q* (orange) is the pulsed

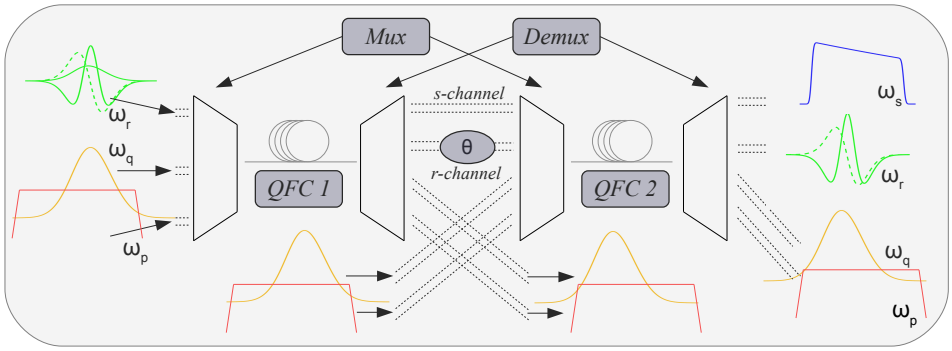

Fig. 5. Illustration of temporal-mode interferometry using two stages of quantum frequency conversion (QFC) in optical fiber. Original input is a superposition of temporal-modes in the *r*-channel (green), and the two pumps *p* (red, continuous-wave/long pulse) and *q* (orange, pulsed). The shape of the pulsed pump decides the target temporal-mode which is to be converted to a signal in the *s*-channel (blue). The intermediate stage contains replacement of the pumps and a variable relative phase shift θ (here on the *r*-channel). Mux and Demux represent wavelength multiplexing and demultiplexing respectively.

#243459 Received 23 Jun 2015; revised 17 Aug 2015; accepted 17 Aug 2015; published 26 Aug 2015

pump which has the approximate shape of the TM which is specified to be converted to a signal in the *s*-channel (blue). The strength of the TMI scheme lies in its ability to convert a single Schmidt mode with 50% CE, while converting all higher-order Schmidt modes with near 0% efficiency (i.e. $\mathscr{S} \approx 1$ when $\rho_1 = 1/\sqrt{2}$). Thus, considering only the target TM after the first QFC stage, it is placed in a color superposition between being frequency converted and not being converted, completely analogous to a Mach-Zender interferometer with conversion and non-conversion corresponding respectively to reflection and transmission at the input beam splitter. Using the output of the first QFC stage as the input to the second QFC stage allows the quantum superposition of the target TM to coherently interfere (phase coherence was demonstrated in [21]) either constructively ($\theta = 0$) or destructively ($\theta = \pi/2$) depending on the relative phases of the participating fields.

For the fields to undergo an additional collision in the second QFC stage, we propose one of the following two possible methods: (i) In the "reverse collision" (RC) configuration, the fiber in the second stage is designed to have its dispersion reversed (local curvature inverted) relative to that of the first, resulting in a second collision between the fields because the inverse group speeds are swapped. The RC configuration might be difficult to implement in practice due to the need for specific dispersion engineered fibers. However, with the recent advancement in photonic crystal fibers, which allow for a wide variety of dispersion profiles, it is feasible. (ii) In the "double collision" (DC) configuration, the two stages consist of identical fibers. To ensure the full collision in the second fiber, the intermediate region introduces a delay of the faster propagating field with respect to the slower propagating field. The DC configuration is superior to the RC configuration with regard to simplicity, but as we shall see, its performance is somewhat inferior in terms of the attainable selectivity.

4.1. Theory

Combining the effects of the two QFC stages, we can readily identify the combined GF kernel for a signal initially in the *r*-channel. The combined GFs are [9]

$$G_{rr}(t,t') = \int_{-\infty}^{\infty} \mathrm{d}t'' \left[G_{rr}^{(2)}(t,t'') \exp(i\theta)\, G_{rr}^{(1)}(t'',t') + G_{rs}^{(2)}(t,t'') G_{sr}^{(1)}(t'',t') \right], \tag{17}$$

$$G_{sr}(t,t') = \int_{-\infty}^{\infty} \mathrm{d}t'' \left[G_{sr}^{(2)}(t,t'') \exp(i\theta)\, G_{rr}^{(1)}(t'',t') + G_{ss}^{(2)}(t,t'') G_{sr}^{(1)}(t'',t') \right], \tag{18}$$

where the superscripts $1,2$ label the stage number, and θ is a phase shift applied to the *r*-channel in agreement with the notation used in Fig. 5. The combined GFs can also be written in terms of the Schmidt decompositions of the individual stages as

$$G_{rr}(t,t') = \sum_{m,n} \left[\tau_m^{(2)} \nu_{mn} \tau_n^{(1)} \exp(i\theta) - \rho_m^{(2)} \mu_{mn} \rho_n^{(1)} \right] \Psi_m^{(2)}(t) \psi_n^{(1)*}(t'), \tag{19}$$

$$G_{sr}(t,t') = -\sum_{m,n} \left[\rho_m^{(2)} \nu_{mn} \tau_n^{(1)} \exp(i\theta) + \tau_m^{(2)} \mu_{mn} \rho_n^{(1)} \right] \Phi_m^{(2)}(t) \psi_n^{(1)*}(t'), \tag{20}$$

where μ_{mn} and ν_{mn} are inter-stage temporal mode overlaps defined as

$$\mu_{mn} = \int_{-\infty}^{\infty} \mathrm{d}t\, \phi_m^{(2)*}(t) \Phi_n^{(1)}(t), \qquad \nu_{mn} = \int_{-\infty}^{\infty} \mathrm{d}t\, \psi_m^{(2)*}(t) \Psi_n^{(1)}(t), \tag{21}$$

and measure the degree to which the output modes of the first stage coincide with the input modes of the second stage. The stages are temporally mode matched if $|\mu_{mn}| = |\nu_{mn}| = \delta_{mn}$, which is possible only if we can write $\phi_m^{(2)}(t) = \exp(i\alpha_1) \Phi_m^{(1)}(t)$ and $\psi_m^{(2)}(t) = \exp(i\alpha_2) \Psi_m^{(1)}(t)$, where $\alpha_{1,2}$ are constants.

#243459 Received 23 Jun 2015; revised 17 Aug 2015; accepted 17 Aug 2015; published 26 Aug 2015

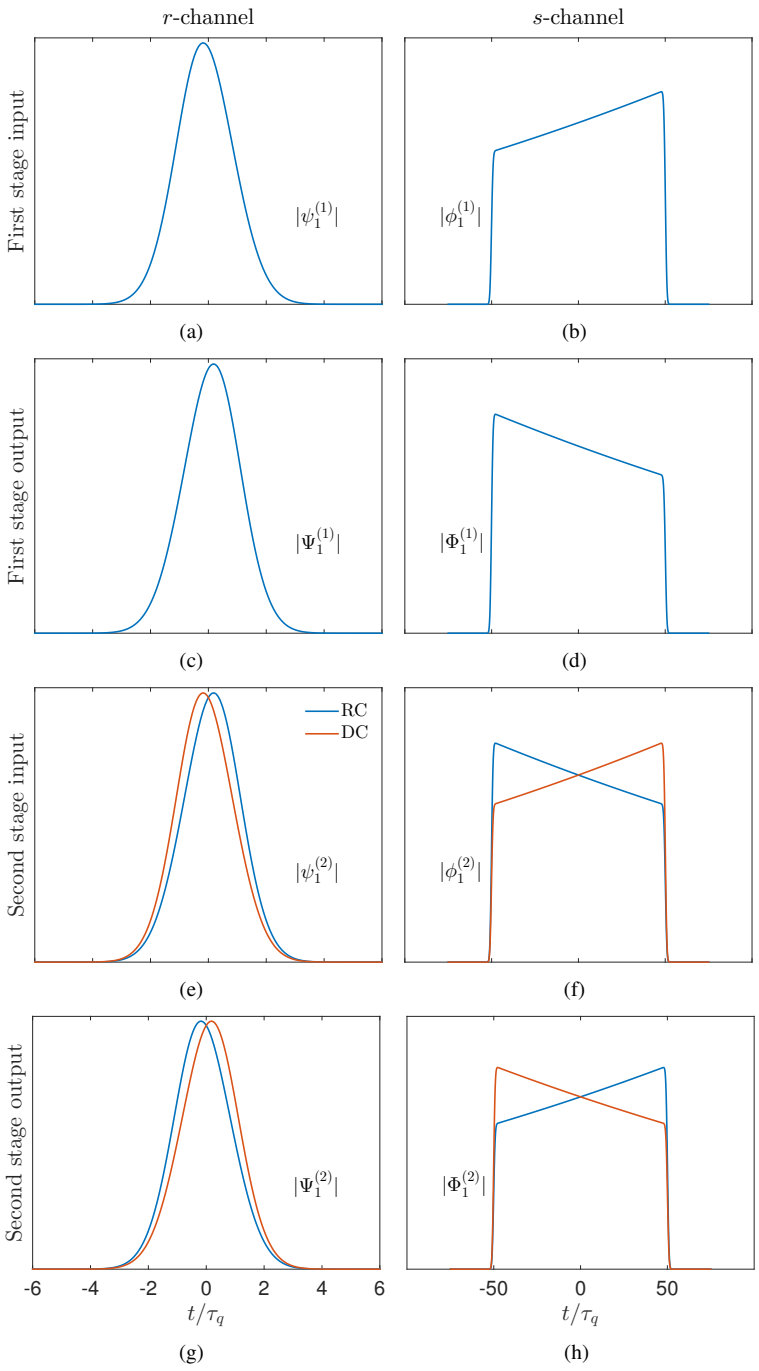

Fig. 6. Schmidt modes of (a,c,e,g) the r-channel and (b,d,f,h) the s-channel for $\gamma' = 0.825$, $\zeta = 50$. All the Schmidt modes have been centered on the normalized time-axis to facilitate comparison. The lack of temporal mode overlap in the DC configuration is apparent when comparing the output Schmidt modes of the first stage in (c,d) with the corresponding input Schmidt modes of the second stage in (e,f). This mismatch is not observed for the RC configuration which is temporally mode matched. The legend in (e) also applies to (f,g,h).

#243459 Received 23 Jun 2015; revised 17 Aug 2015; accepted 17 Aug 2015; published 26 Aug 2015

To understand the implications of Eqs. (19) and (20), consider an input in the r-channel given by a scalar multiplied by a specific Schmidt mode $A_r^{\text{in}}(t') = a_n \psi_n^{(1)}(t')$ and the s-channel initially empty $A_s^{\text{in}}(t') = 0$. The outputs after the two stages are then given using Eqs. (4), (14), (19), and (20) as

$$A_r^{\text{out}}(t) = a_n \sum_m \left[\tau_m^{(2)} \nu_{mn} \tau_n^{(1)} \exp(i\theta) - \rho_m^{(2)} \mu_{mn} \rho_n^{(1)} \right] \Psi_m^{(2)}(t), \tag{22}$$

$$A_s^{\text{out}}(t) = -a_n \sum_m \left[\rho_m^{(2)} \nu_{mn} \tau_n^{(1)} \exp(i\theta) + \tau_m^{(2)} \mu_{mn} \rho_n^{(1)} \right] \Phi_m^{(2)}(t). \tag{23}$$

Ideally, the target mode $n = 1$ is fully converted, $|A_s^{\text{out}}(t)| = a_1 \Phi_1^{(2)}(t)$, and non-target modes $n > 1$, are fully transmitted $|A_r^{\text{out}}| = a_n \Psi_n^{(2)}(t)$, without cross-talk between different temporal modes. This situation is obtainable for a specific value of θ, provided that (i) the two QFC stages are temporally mode matched for equal mode orders, i.e. $|\mu_{mn}| = |\nu_{mn}| = \delta_{mn}$, (ii) the target mode is 50% frequency converted in both stages i.e. $\rho_1^{(1,2)} = \tau_1^{(1,2)} = 1/\sqrt{2}$, and (iii) none of the non-target modes are frequency converted in either of the stages i.e. $\tau_{n\geq 2}^{(1,2)} = 1$. Using TMI we relax the last requirement to convert all non-target modes with only low probability in both stages [review Fig. 4(b)].

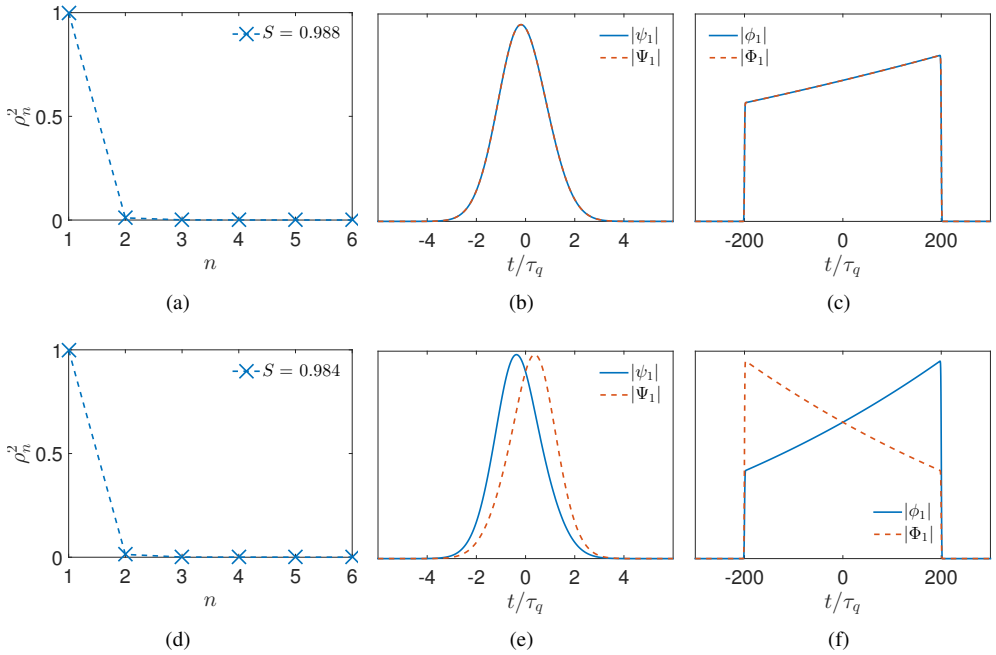

Fig. 7. Schmidt decomposition of the two-stage combined Green function G_{sr} for (a-c) RC and (d-f) DC configurations using $\gamma' = 0.825$ and $\zeta = 200$. (a,d) show the values of the six lowest Schmidt coefficients, (b,e) show the r-channel Schmidt modes, and (c,f) show the s-channel Schmidt modes.

#243459 Received 23 Jun 2015; revised 17 Aug 2015; accepted 17 Aug 2015; published 26 Aug 2015

4.2. *Results*

Figure 6 shows the full set of first-order Schmidt modes (centered on the normalized time axis) for the first QFC stage and the second QFC stage, including both RC and DC configurations. It appears that the RC configuration naturally results in perfect temporal mode matching between the output modes from the first stage and the input modes of the second stage. On the other hand, this is not the case for the DC configuration as the Schmidt modes are oppositely skewed. Furthermore, for DC, a non-converted state which is input in either the *r*- or the *s*-channel seems to be temporally distorted when sent through the device, resulting in a potential issue in cases where cascaded TMI devices are required. This is not the case using RC, where the output state of a non-converted TM maintains its initial form, and is thus undistorted by the device.

Temporal-mode overlap between the output modes from the first stage and the input modes from the second stage is necessary, but not sufficient, to obtain an interferometric effect between the two stages; the phase profiles must also match. To see why this is not initially the case, review the GF kernels in Eqs. (5)–(8). The complex phase terms, which are linear in t $(-t')$, are separable, and therefore directly transfer to the Schmidt modes, destroying the temporal mode matching. Fortunately, we can utilize the form of the GF kernel to remove the time-varying complex exponential. This is done by a simple carrier frequency shift of both pumps by the amount $\omega = +\Gamma_p$ ($\omega = -\Gamma_p$ in the second stage of RC). Since the pumps are frequency shifted in the same direction, energy conservation is still obeyed, and furthermore if the frequency shift is small, we can consider it as a small perturbation to the original equations, which does not alter our solution. With these considerations taken into account, Fig. 7 shows the lowest-order Schmidt coefficients, and the first-order input/output Schmidt modes for the combined GF, for (a-c) the RC case and (d-f) the DC case. As shown in the legends of the plots including the Schmidt coefficients, we obtain $S = 0.988$ for RC, and slightly lower $S = 0.984$ for DC. The smaller selectivity in the DC case, results from a non-perfect temporal mode match of $|\eta_{11}| = |\mu_{11}| = 0.981$, whereas $|\eta_{11}| = |\mu_{11}| = 1$ for RC.

In Fig. 8, we show the dual-stage selectivity versus γ' for selected values of ζ. Apparently the value of γ' that yields maximum selectivity is extremely robust against changes in ζ, with the maximum found at $\gamma' = 0.825$. This is a useful result enabling the choice of pump power P_p and

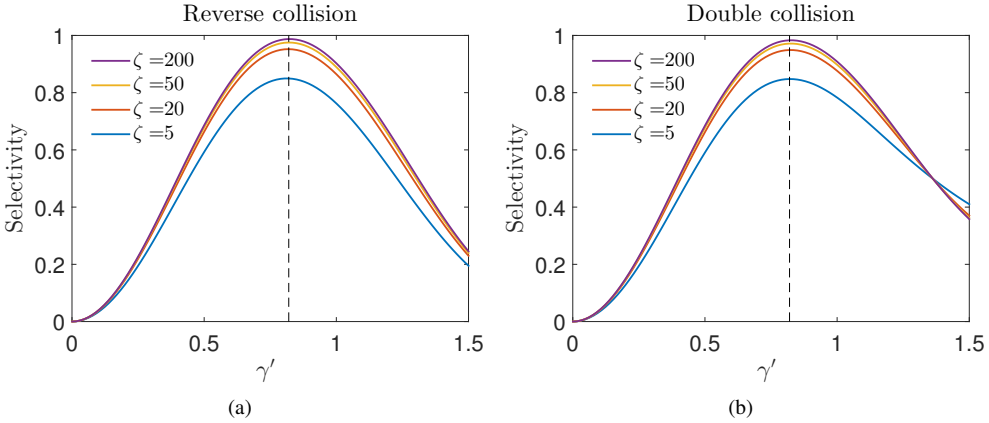

Fig. 8. Dual-stage selectivity versus γ' for (a) the RC configuration and (b) the DC configuration. The maximum selectivity point is obtained for $\gamma \approx 0.825$ (dotted line), exhibiting stable behavior against variation in ζ.

#243459 Received 23 Jun 2015; revised 17 Aug 2015; accepted 17 Aug 2015; published 26 Aug 2015

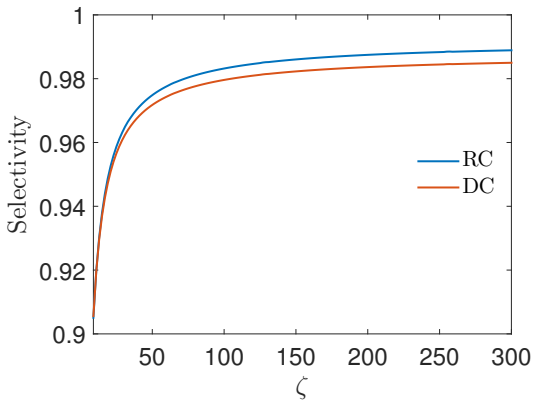

Fig. 9. Dual-stage selectivity versus the dimensionless fiber length ζ for $\gamma' = 0.825$.

pulse energy E_q, given the fiber parameters γ, β_{rs}, and l, so as to obtain maximum selectivity. Additionally, we must seek to make ζ as large as possible to minimize the CE of non-target TMs, as demonstrated in Fig. 9. The selectivity increases dramatically for values $\zeta < 50$, after which it goes only asymptotically to unity. The 0.98-selectivity point is crossed at $\zeta \approx 70$ for RC, and at $\zeta \approx 100$ for DC.

4.3. Numerical analysis and feasibility

The analysis performed until this point, which predicts excellent TM selectivity, has neglected the effect of NPM from pump q, assuming it to be considerably weaker than pump p. However, it is not obvious that a scheme such as TMI, which relies highly on the phase profiles of the signals, is not extremely sensitive to small phase variations. For this reason, we have performed extensive numerical calculations using a Runge-Kutta split-step method to solve the full set of coupled-mode equations in Eq. (1). We have used the method presented in [4, 9] to find the singular value decomposition of the GF kernel G_{sr}. For completeness, the effect of intra-pulse dispersion was included using the dispersion profile from a specific solid-core photonic crystal fiber.

In the theoretical analysis pump p was a CW field, but modeling it as such was not appropriate for the numerical scheme used, and in reality the power levels would be limited due to stimulated Brillouin scattering. Instead, we now model pump p as a broad square-like pump pulse of duration exceeding the difference in transit time between the pulses by a factor of 5. In the present analysis the full-width of the broad pump is approximately 300 ps, while the e^{-1}-width of the Gaussian pump q is 1 ps.

To reduce the potential influence of Raman scattering, the two pumps are placed on the low-frequency side of the zero-dispersion wavelength, which for the considered photonic crystal fiber is at 736 nm. Furthermore, the broader pump p is placed at the lowest frequency, at a frequency shift from the narrow pump q that exceeds the Raman peak of the specific waveguide material (at $\Delta\nu \approx 13$ THz for silica).

It only remains to discuss the required physical parameters needed in order to obtain good selectivity. The theory predicts that $\zeta = \beta_{rs} l/(2\tau_q)$ has to be maximized, while the nonlinear interaction strength $\gamma' = \gamma\sqrt{P_p E_q l/\beta_{rs}}$ is optimal at around 0.825. However, by including the effect of NPM from pump q, we also want to minimize the resulting peak phase shift on the signals, which is estimated by the quantity $\theta_q = \gamma l |A_q|^2_{\max}$, so that it is small as compared to 2π. The restriction on the interaction strength γ' implies the proportionality $\theta_q \propto \beta_{rs}/(\gamma P_p \tau_q)$, which

#243459 Received 23 Jun 2015; revised 17 Aug 2015; accepted 17 Aug 2015; published 26 Aug 2015

stresses the need of a high power in pump p. Using $\gamma = 2\gamma_K = 0.2$ W^{-1} m^{-1}, $P_p = 30.0$ W, $E_q = 5.52 \times 10^{-14}$ J, $\beta_{rs} = 2.92 \times 10^{12}$ s m^{-1}, and $l = 30.0$ m, it was possible to achieve a selectivity of $S = 0.977$ in a full simulation for the DC configuration. The value of θ_q was 0.06π, and the frequency shifts applied to the pumps prior to the two stages were $\Gamma_p = 2.06 \times 10^{12}$ rad s^{-1} corresponding to wavelength shifts on the order of $\Delta\lambda \sim -0.5$ nm.

5. Conclusion

We have for the first time presented the full set of analytical Green function kernels describing frequency conversion by asymmetrically-pumped Bragg scattering, and used them to show that dual-stage temporal-mode interferometry achieves nearly perfect temporal-mode sorting with selectivities reaching $S \sim 0.99$. Comparable results have been reported for four-wave mixing using two pulsed pumps, though to match the inter-stage temporal mode profiles, challenging pump pre-chirps were necessary. Using asymmetrically-pumped Bragg scattering, greatly simplifies the operation as the challenging pre-chirps are replaced by pre-stage frequency shifts ($\Delta\lambda \sim 0.5$ nm) of the pump carrier frequencies.

In asymmetrically-pumped Bragg scattering the nonlinear interaction is caused by a strong constant-amplitude pump, while a weak pump merely defines the target temporal mode by virtue of its pulse shape. The asymmetry of the two pumps results in an imitation of three-wave mixing, which is also promising with respect to achieving high selectivies in a temporal-mode interferometry setup. However, the three-wave mixing scheme lacks fiber-mode compatibility, it does not allow for small frequency shifts, and it is limited with respect to pulse walk-off due to available lengths of second-order nonlinear crystal waveguides. Asymmetrically-pumped Bragg scattering does not suffer from these limitations, and should therefore find its uses where one or multiple of these effects are crucial for the application.

Two forms of temporal-mode interferometry were reviewed: the "reverse collision" and the "double collision" configurations, and the reverse collision configuration was found to be superior due to non-unity inter-stage temporal-mode overlap in the double collision configuration. However, the double collision configuration allows for a much simpler setup, and is therefore essential for initial experiments.

The analytical model presented, relies on neglecting nonlinear phase modulation from the weaker and short duration pump. We showed that high selectivity ($S > 0.97$) using temporal-mode interferometry is still achievable, even when nonlinear phase modulation from the second pump is included, albeit at the cost of needing a high peak power in the strong pump (~ 30 W). Our work enables the first proof-of-concept-demonstrations e.g. using parameters comparable to those suggested in the final part of this paper.

Acknowledgments

JC was funded by Østsjællands Andelsvaskeris Fond, Knud Højgaards Fond, and Henry og Mary Skovs Fond. DR and MR were supported by the National Science Foundation through EPMD and GOALI, Grant No. ECCS-1101811.

#243459 Received 23 Jun 2015; revised 17 Aug 2015; accepted 17 Aug 2015; published 26 Aug 2015